

## Real-space multiple-scattering calculation and interpretation of x-ray-absorption near-edge structure

A. L. Ankudinov

*MST-11, Los Alamos National Laboratory, Los Alamos, New Mexico 87545*

B. Ravel

*Ceramics Division, National Institute of Standards and Technology, Gaithersburg, Maryland 20899*

J. J. Rehr

*Department of Physics, University of Washington, Seattle, Washington 98195-1560*

S. D. Conradson

*MST-11, Los Alamos National Laboratory, Los Alamos, New Mexico 87545*

(Received 26 September 1997; revised manuscript received 14 April 1998)

A self-consistent real-space multiple-scattering (RSMS) approach for calculations of x-ray-absorption near-edge structure (XANES) is presented and implemented in an *ab initio* code applicable to arbitrary aperiodic or periodic systems. This approach yields a quantitative interpretation of XANES based on simultaneous, self-consistent-field (SCF) calculations of local electronic structure and x-ray absorption spectra, which include full multiple scattering from atoms within a small cluster and the contributions of high-order MS from scatterers outside that cluster. In addition, the code includes a SCF estimate of the Fermi energy and an account of orbital occupancy and charge transfer. We also present a qualitative, scattering-theoretic interpretation of XANES. Sample applications are presented for cubic BN,  $\text{UF}_6$ , Pu hydrates, and distorted  $\text{PbTiO}_3$ . Limitations and various extensions are also discussed. [S0163-1829(98)03736-9]

### I. INTRODUCTION

X-ray-absorption near-edge structure (XANES) refers to the region of the x-ray absorption spectroscopy (XAS) spectrum dominated by strong photoelectron scattering that extends about 40 eV above an absorption edge. XANES is currently of great interest in many scientific fields due to its promise of providing local chemical information in complex and disordered materials. However, both the calculation and interpretation of XANES have remained challenging problems.<sup>1,2</sup> Although the fundamental multiple-scattering (MS) formalism of x-ray absorption is well established,<sup>3,4</sup> current computational techniques are often unsatisfactory for large aperiodic systems. Currently available full-MS XANES codes<sup>1</sup> are of limited accuracy due to large basis size requirements and the lack of self-consistent-field (SCF) potentials, while conventional ground-state electronic structure methods<sup>5</sup> usually depend on lattice periodicity or neglect core-hole and self-energy effects. Moreover, the interpretation of XANES in terms of electronic structure alone is indirect, making a quantitative interpretation difficult. Consequently, XANES is typically interpreted only qualitatively. This is in contrast to the weak-scattering region above about 40 eV of an edge—the extended x-ray-absorption fine-structure (EXAFS) region—for which accurate finite MS calculations and a geometrical interpretation are now standard.<sup>6</sup>

In an attempt to remedy these difficulties we present here a SCF real-space multiple-scattering (RSMS) theory<sup>7</sup> of XANES for arbitrary systems without any requirement of symmetry or periodicity. Our goal in this paper is to present a quantitative interpretation of XANES based on simulta-

neous calculations of XAS and electronic structure such as the electronic densities of states (DOS) and charge counts. Our approach is based on cluster calculations of the single-particle Green's function, the central ingredient in both electronic structure and XANES calculations. An advantage of RSMS with respect to other electronic structure methods is that it uses an integration in the complex energy plane to sum over occupied states and hence avoids an explicit determination of energy eigenstates. Our method partly avoids the difficulties of large clusters by using full MS calculations to obtain the contribution to the Green's function from a small cluster—typically less than 100 atoms—and a high-order MS expansion for important paths that extend outside this small cluster. In addition, we present an XAFS-like scattering theoretic interpretation of XANES that connects the spectrum to structural and chemical information. Our method is implemented in a semiautomated, relativistic code FEFF8, based partly on efficient algorithms from earlier versions of our *ab initio* XAFS codes FEFF.<sup>6</sup> We also present several comparisons of this approach to experiment and to other theories to test its validity.

The organization of this paper is as follows. In Sec. II, we describe our RSMS approach for SCF calculations of DOS and XANES. In Sec. III, we present several applications to demonstrate the effect of self-consistency on XANES and DOS calculations and to illustrate the advantages and limitations of our method. In Sec. IV, we present a scattering theoretic interpretation. Finally, in Sec. V we give several conclusions. Additional applications will be discussed elsewhere.

## II. THEORY

The physical quantity of interest in XAS is the x-ray-absorption coefficient  $\mu(E)$ . A close connection between XAS and electronic structure is indicated by the similarity between the contribution to the XAS from a given site  $i$  and orbital angular momentum  $l$  and the local  $l$ -projected electronic density of states (LDOS) at site  $i$ ,<sup>3</sup>

$$\begin{aligned}\mu_{li}(E) &= \mu_{li}^{0'}(E)[1 + \chi'_{li}(E)], \\ \rho_{li}(E) &= \rho_{li}^0(E)[1 + \chi_{li}(E)],\end{aligned}\quad (1)$$

where  $\mu_{li}^{0'}(E)$  and  $\rho_{li}^0(E)$  are the smoothly varying atomic background contributions and  $\chi_{li}(E)$  [or  $\chi'_{li}(E)$ ] is the fine-structure or XAFS spectrum. In Eq. (1) and elsewhere, when needed for clarity, we will use a prime to denote final-state quantities calculated in the presence of a screened core hole. Because of the similarity between  $\mu_{li}(E)$  and  $\rho_{li}(E)$ , it is widely thought that XAS directly measures the LDOS.<sup>5</sup> However, this interpretation can be misleading because of the importance of the core hole in the calculation of XAS. Explicit examples of this will be shown in Sec. III. Thus, a quantitative interpretation of XAS generally requires calculations both with and without a core hole.

Calculations both of XAS and the LDOS in aperiodic systems are efficiently carried out within a RSMS Green's-function formalism,<sup>3,4,7</sup> which is a real-space analog of the Koringa-Kohn-Rostoker (KKR) band-structure method. Similar MS formalisms are the basis for many cluster approaches to XANES calculations.<sup>1</sup> However our approach has several advantages as discussed below.

The spatial and energy dependence of the electron DOS can be expressed in terms of the imaginary part of the one-electron Green's-function operator  $G = [E - H]^{-1}$ , where  $H$  is the effective one-electron Hamiltonian and  $E$  is the (generally complex) photoelectron energy. In our approach, we always calculate the retarded Green's function, which is an analytic function in the upper half  $E$  plane. For example the total DOS  $\rho(E)$  for real energies  $E$  is given by the integral of  $\text{Im } G$  in position space,

$$\rho(E) = -\frac{2}{\pi} \text{Im} \int d^3r G(\mathbf{r}, \mathbf{r}, E), \quad (2)$$

where  $G(\mathbf{r}', \mathbf{r}, E) = \langle \mathbf{r}' | G(E + i\eta) | \mathbf{r} \rangle$ , and  $\eta = 0+$ . The factor of 2 accounts for spin degeneracy and the Fermi level  $E_F$  is found by requiring a fixed number of electrons in occupied states below  $E_F$ . The total electron density is then given by

$$\rho(\mathbf{r}) = -\frac{2}{\pi} \text{Im} \int_{-\infty}^{E_F} dE G(\mathbf{r}, \mathbf{r}, E). \quad (3)$$

By using analytic properties of  $G$ , the integral can be evaluated around any contour  $C$  in the upper half of the complex  $E$  plane with the same initial and final points. We use this property to simplify the calculations, since the spectral quantities of interest are much smoother above the real axis. In our calculations we use frozen core states, though in principle the core wave functions could be recalculated during the SCF loop. Thus, for the valence electron density, the integral in Eq. (3) should be carried out from an initial en-

ergy  $E_c$  above all core energy levels and below all valence states. By using a rectangular contour  $C$  the integration is stable, and it is usually adequate to use only 60–100 points for the entire valence region, which typically extends about 40 eV below the Fermi level.

Both the x-ray absorption and emission spectra can be calculated from the same one-particle Green's function. From Fermi's golden rule and the one-electron and dipole approximations, the x-ray absorption coefficient is given by  $\tilde{\mu}(E) \propto \sum_f |\langle f | \hat{\mathbf{e}} \cdot \mathbf{r} | i \rangle|^2 \delta(E - E_f)$ , where  $\hat{\mathbf{e}}$  is the x-ray polarization vector,  $|i\rangle$  is an initial core state, and  $|f\rangle$  is a final state. Lifetime broadening is ignored in  $\tilde{\mu}(E)$  but will be added as discussed below. Using the spectral representation  $\sum_f |f\rangle \delta(E - E_f) \langle f| = (-1/\pi) \text{Im } G(E)$ , the golden rule becomes

$$\tilde{\mu}(E) \propto -\frac{2}{\pi} \text{Im} \langle i | \hat{\mathbf{e}} \cdot \mathbf{r}' G(\mathbf{r}', \mathbf{r}, E) \hat{\mathbf{e}} \cdot \mathbf{r} | i \rangle, \quad (4)$$

where  $E$  is real. The effects of core-hole lifetime and experimental broadening effects may be included using a convolution. Since only transitions to unoccupied levels above  $E_F$  are allowed, we have

$$\mu(E) = \int_{E_F}^{\infty} dE' \tilde{\mu}(E') \frac{\Gamma}{\pi[(E - E')^2 + \Gamma^2]}, \quad (5)$$

where  $\Gamma$  is determined by the combined sum of the core-hole lifetime and experimental resolution. In this formula the threshold level  $E_F$  (as well as the SCF DOS and charge density) is usually calculated in the presence of a screened core hole, in accordance with the final-state rule. In our treatment this corresponds to a fully relaxed core hole. We remark that to obtain the x-ray emission spectra (XES), we need only change the limits of the convolution to  $(-\infty, E_F)$ , the energy range corresponding to the occupied states. However, since the valence-band DOS often has sharp peaks due to quasibound states, it may be preferable to carry out calculations of XES in the complex  $E$  plane. Thus, using the analyticity in  $E$  of  $G$  (and  $\tilde{\mu}$ ), the integral in Eq. (5) can be done along any contour  $C$  in the upper-half complex  $E$  plane with the same initial and final points that goes below the pole of the integrand at  $E' = E + i\Gamma$ . For example, the integration can be done along the contour  $C$ , which goes from  $-\infty + i\Gamma/2$  to  $E_F + i\Gamma/2$  to  $E_F$ . Such a contour can be used to calculate XES with much larger steps in energy than if the integral were evaluated along the real axis.

In this paper we present two key developments for XAS calculations for arbitrary systems and their interpretation in terms of local electronic structure: (1) the use of SCF potentials and (2) the use of full MS (FMS) cluster calculations of both XAS and DOS calculations. Both of these developments are based on Green's-function calculations in the complex plane. The SCF procedure permits an *ab initio* calculation of the threshold or Fermi energy as well as an evaluation of occupation numbers and charge transfer between ions in the cluster, an effect not usually included in most previous XAS calculations.<sup>1,6</sup> The FMS approach is necessary for an accurate calculation of XANES when the MS path expansion fails to converge rapidly, i.e., when  $|\chi|$  is not small compared to unity. Although other XANES codes are based on FMS

cluster calculations,<sup>1</sup> to our knowledge, ours is the first such code that also includes simultaneous calculations of electronic structure.

These two developments are implemented as extensions to previous versions of our semiautomated FEFF codes.<sup>6</sup> In the remainder of this section, we describe in detail the SCF loop used to compute the electron density and scattering potential within our RSMS framework. As suggested by Eq. (1), calculations of XAS and DOS are similar in that they are related to similar Green's functions. The significant distinction is that the calculation of  $\chi'(E)$  needed for XAS must be computed for final states in the presence of a core hole and must include self-energy and thermal corrections, whereas  $\chi(E)$  for the DOS and electronic structure interpretations is usually that for the ground state. In practice, a single SCF calculation of  $G(E)$  for a suitably large cluster is sufficient to calculate  $\chi(E)$  both with and without the core hole, since our calculations are typically done for a cluster sufficiently large that it contains both an absorber with a core hole and neutral atoms of the same atomic species. The quantity  $\mu(E)$  also requires a calculation of embedded-atomic dipole matrix elements  $\mu^0(E)$ ,<sup>8</sup> i.e., matrix elements between atomiclike states calculated with SCF (or overlapped atom potentials) that include solid-state corrections. In this work, we neglect many-body effects due to intrinsic and extrinsic excitations and their interference,<sup>9</sup> that is, shake-up and shake-off processes. These effects are usually approximated by a multiplicative factor  $S_0^2(E)$  in  $\chi(E)$ , which depends weakly on energy. Efforts to improve on this approximation are in progress.

The RSMS method is formally similar to the  $k$ -space KKR band-structure approach and the real-space  $X\alpha$  MS approach,<sup>10</sup> since both were originally based on muffin-tin (MT) MS theory. However, in the KKR and  $X\alpha$  methods, discrete wave functions are calculated using the Lippman-Schwinger equation, while in the RSMS method, the electron Green's function is calculated, which implicitly sums over all one-particle states. Although our RSMS calculation of  $G$  uses a MT potential, the MT approximation is not inherent to the RSMS technique and an extension of the method to full potentials would be desirable. Even though many modern band-structure codes use full-potential generalizations, we felt that the lack of self-consistency was the more serious approximation made in most currently available XANES codes and should be corrected first. Nonspherical corrections to the potentials can be roughly approximated by allowing the MT spheres to overlap. Though less precise than full-potential methods, such overlapping MT potentials may be adequate for XANES calculations, due both to finite experimental resolution and the fact that errors in the interstitial potential are of decreasing importance with energy above  $E_F$ .

To initialize the SCF loop we use our single-configuration Dirac-Fock atomic code<sup>6</sup> to obtain free atomic densities and then the overlapped atom (Mattheiss) prescription<sup>11</sup> for the total electronic density and Coulomb potential. For all iterations we use the ground-state von Barth-Hedin exchange-correlation potential.<sup>12</sup> Next, we approximate the total potential with a MT potential, which is flat in the interstitial region and otherwise is equal to the sum of overlapping, spherically symmetric potentials,  $V_{\text{tot}}(\mathbf{r}) \approx V_{\text{mt}} + \sum_i V_i(|\mathbf{r} - \mathbf{R}_i|)$ . The MT

radii are determined using the Norman prescription as in our FEFF7 code,<sup>6</sup> and are not changed after the initial iteration. We also reserve the option in our code to use overlapping MT radii for severe cases, when nonoverlapping spheres lead to worse agreement with experiment. MS theory has not been rigorously proved for the case of overlapping MT spheres, but has been found empirically to give better results for such severe cases. We add to the total potential the Hedin-Lundqvist (HL) energy-dependent self-energy<sup>13</sup> correction only for XAS calculations and only after the SCF loop is finished.

In the next step of the SCF loop, we solve the Dirac equation in the spinor relativistic approximation<sup>14</sup> for the above MT potentials to obtain radial wave functions and partial wave phase shifts. These quantities are used in turn to construct the Green's function, which consists of a central atom and scattering contributions:

$$G(\mathbf{r}, \mathbf{r}', E) = G^c(\mathbf{r}, \mathbf{r}', E) + G^{\text{SC}}(\mathbf{r}, \mathbf{r}', E), \quad (6)$$

$$G^{\text{SC}}(\mathbf{r}, \mathbf{r}', E) = -2p \sum_{L, L', \alpha} R_L^\alpha(\mathbf{r}) G_{Lc, L'c}^{\text{SC}}(E) R_{L'}^\alpha(\mathbf{r}'), \quad (7)$$

$$G^c(\mathbf{r}, \mathbf{r}', E) = -2p \sum_{L, \alpha} R_L^\alpha(r_<) [N_L^\alpha(r_>) + iR_L^\alpha(r_>)] \times Y_L(\hat{r}) Y_L^*(\hat{r}'), \quad (8)$$

where  $p = \sqrt{2(E - V_{\text{mt}})}$  and Hartree atomic units  $e = \hbar = m = 1$  are used. Here  $R_L^\alpha$  and  $N_L^\alpha$  are the regular and irregular solutions of the Dirac equation for the spherically symmetric potential and  $R_L^\alpha(\mathbf{r}) = i^l e^{i\delta_l} R_L^\alpha(r) Y_{lm}(\hat{r})$ , and  $L = (lm)$ . The index  $\alpha$  labels the spinor components; the upper component is normalized to  $\sin(pr + \delta_l - l\pi/2)$  as  $r \rightarrow \infty$ . We also include an additional relativistic normalization factor that is typically close to unity. The introduction of the index  $\alpha$  is the only difference from the corresponding nonrelativistic expression, where  $R_l$  would denote a solution of the Schrödinger equation. A simple summation over  $\alpha$  is adequate for the density calculations. The lower Dirac component may be neglected in the interstitial region, but must be kept for accurate charge calculations in the deep core region.<sup>14</sup>

The scattering contribution  $G_{Lc, L'c}^{\text{SC}}(E)$  may be expressed formally by the MS path expansion<sup>15</sup> in terms of the two center matrix elements of the free propagator  $G^0$  and the scattering  $t$  matrix,

$$G_{Lc, L'c}^{\text{SC}}(E) = \sum_i G_{Lc, L_1 i}^0 t_{L_1 i} G_{L_1 i, L'c}^0 + \sum_{i_1, i_2} G_{Lc, L_1 i_1}^0 t_{L_1 i_1} G_{L_1 i_1, L_2 i_2}^0 t_{L_2 i_2} G_{L_2 i_2, L'c}^0 + \dots, \quad (9)$$

where summation over intermediate angular momentum indices is implied. Here the two center propagators and scattering matrices are defined as

$$G_{Li, L'i'}^0 = (1 - \delta_{i, i'}) G_{L, L'}^0(\mathbf{R}), \quad (10)$$

$$t_{Li,L'i'} = \delta_{i,i'} \tilde{\delta}_{L,L'} t_l, \quad (11)$$

where the index  $i$  denotes the atomic site in the cluster,  $l$  is the orbital angular momentum index, and  $\mathbf{R} = \mathbf{R}_i - \mathbf{R}_{i'}$ . These definitions build in summation restrictions that prohibit the photoelectron from scattering from the same atom twice in a row in a MS path of any order. For the FMS calculations in this work we use exact separable propagators  $G_{L,L'}^0(\mathbf{R}) = (e^{ipR}/pR) \sum_{\lambda} \tilde{Y}_{L\lambda}(\hat{\mathbf{R}}) Y_{L\lambda}(\hat{\mathbf{R}})$  where  $p$  is the complex momentum. These propagators are calculated using the exact Rehr-Albers (RA) algorithm,<sup>15</sup> rather than the finite RA expansion used in FEFF,<sup>6</sup> but are calculated with the same subroutines. The exact RA algorithm has been shown<sup>16</sup> to be both stable and superior in accuracy compared to other constructions. We remark that these matrices are based on dimensionless  $G^0$  and  $t$ , i.e.,  $G^0(\mathbf{r}, \mathbf{r}', E) = -\exp(ip|\mathbf{r} - \mathbf{r}'|)/4\pi p|\mathbf{r} - \mathbf{r}'|$ , and, for spherically symmetric potentials,  $t_l = \exp(i\delta_l) \sin \delta_l$ .<sup>15</sup> These quantities are sometimes defined with an additional factor  $-2p$ , but this cancels in the product  $G^0 t$  encountered in the MS series. For brevity we will often omit angular-momentum or site indices and intermediate summations, as is typically done with matrices, since these indices are easy to restore. For example, the shorthand form of Eq. (9) is

$$G^{\text{SC}} = G^0 t G^0 + G^0 t G^0 t G^0 + \dots \quad (12)$$

In general the finite, high-order MS path expansion has been found to converge well at high energies,<sup>6,17</sup> but can fail in the XANES region in cases of strong scattering. Strong scattering is characterized by large values of the XAFS function  $\chi$ , e.g., when either the largest eigenvalue of  $G^0 t$  or the quantity  $f_{\text{eff}}/pR$  for a given path exceeds unity, where  $f_{\text{eff}}$  is the effective scattering amplitude.<sup>15</sup> Typically, nonconvergence is due to large MS contributions from short bonds at small photoelectron momentum  $p$ . This leads to the appearance of strong peaks in the XANES such as ‘‘white lines’’ and ‘‘shape resonances.’’<sup>2</sup> To handle these cases we apply the FMS method to a finite cluster around the central atom. In FMS treatments, the MS series in Eq. (9) is summed implicitly to all orders by matrix inversion,

$$G^{\text{SC}} = G^0 (1 - t G^0)^{-1} = (1 - G^0 t)^{-1} G^0. \quad (13)$$

For both XAS and DOS the quantity of interest is the submatrix of  $G_{Li,L'i'}$  for which  $i$  and  $i'$  both refer to an absorbing atom in the XAS calculation or a central atom in a DOS calculation. Because the partial wave phase shifts decay exponentially with increasing  $l$  beyond  $(l_{\text{max}} + 1) \sim kr_{\text{mt}}$ , where  $r_{\text{mt}}$  is the MT radius of the central atom,  $G^{\text{SC}}$  can be calculated with reasonable computer resources for energies smaller than of order  $[(l_{\text{max}} + 1)/r_{\text{mt}}]^2$  Ry and sufficiently small clusters, e.g., to about 30 eV for  $r_{\text{mt}} \approx 2-3$  bohr and  $l_{\text{max}} = 2$ . The time required for the matrix inversion in Eq. (13) scales as the cube of the dimension  $N(l_{\text{max}} + 1)^2$  of  $G^{\text{SC}}$ , where  $N$  is the number of atoms in the cluster. Because of this strong dependence on dimensionality, calculations in the XANES region are typically limited to fairly small clusters of order 100 atoms on modern workstations. In practice, clusters of this size appear to be adequate in many cases, as

will be demonstrated in Sec. III. Larger clusters can be handled approximately by a combined FMS/high-order MS approach, as discussed below.

Unlike the path-by-path MS expansion, effects of lattice vibrations can only be taken into account approximately in the FMS technique. In our approach we simply append a factor  $\exp(-\sigma_{ii'}^2 k^2)$  to each free propagator  $G_{Li,L'i'}^0$ . This procedure yields the correct thermal Debye-Waller factors only for the dominant single scattering terms in the harmonic approximation. Though these thermal factors for the MS paths are not exact, they are reasonable approximations, and can significantly improve convergence.

The CPU time spent in the FMS-SCF loop is currently a bottleneck in our code. It is inconvenient to do SCF calculations for more than 150 atoms on modern workstations as such calculations presently take several CPU hours. We have introduced several algorithms to improve the efficiency. First, we have found that SCF potentials can be calculated to sufficient accuracy with much smaller clusters than the XANES, e.g., clusters of about 30 atoms containing only up to third neighbors about each unique site. Then the main bottleneck becomes the single FMS calculation for a big cluster. To handle even bigger clusters without significant loss of accuracy, we use a combined FMS/high-order MS approach. That is, we treat paths within a given cluster  $C$  surrounding the absorbing atom to all orders and simply add MS paths that extend outside  $C$  by FEFF's high-order MS path expansion and path filters. A possible improvement on this approach is to repartition the matrix  $G^{\text{SC}}$  as follows:

$$G^{\text{SC}} = (1 - G^0 t^C)^{-1} G_0 [t^{\bar{C}} + t^{\bar{C}} G^0 t^{\bar{C}} + t^{\bar{C}} G^0 t G^0 t^{\bar{C}} + \dots] \\ \times G^0 (1 - t^C G^0)^{-1}, \quad (14)$$

where  $t^C$  and  $t^{\bar{C}}$  correspond to scattering from atoms inside the cluster  $C$  and outside  $\bar{C}$  the cluster, and  $t = t^C + t^{\bar{C}}$ . Thus, two matrix inversions should in general be made, but if we can neglect spin or spin-orbit interaction (which is usually the case), only one inversion will be needed, since the two matrices will be simply related. Notice that the scattering paths inside the square brackets should start and end outside the cluster  $C$ , but intermediate atoms could also be inside that cluster. This approach represents a different repartitioning of the MS expansion from that of Fujikawa.<sup>18</sup> Fujikawa also suggested that, in the case of short bond distances between atoms  $i$  and  $j$ , a FMS calculation be made for the simplest two-atom cluster of atoms  $i$  and  $j$ . Then  $\tilde{G}_{ij}^0 = (1 - G_{ij}^0 t_j - G_{ji}^0 t_i)^{-1} G_{i,j}^0$ , which corresponds to the inclusion of full MS between pairs of atoms  $i$  and  $j$ . Actually, both repartitioning schemes can be used simultaneously, since including  $\tilde{G}$  into Eq. (14) is straightforward and leads to a modified single scattering term,

$$G^{\text{SC}} = (1 - G^0 t^C)^{-1} \tilde{G}^0 t^{\bar{C}} \tilde{G}^0 (1 - t^C G^0)^{-1} \\ + \sum_{ij} (1 - G^0 t^C)^{-1} \tilde{G}_{c,i}^0 t_{i,j}^{\bar{C}} (G^0 - \tilde{G}^0)_{j,i} (1 - t^C G^0)^{-1}_{i,c}, \quad (15)$$

where atoms  $c$  and  $i$  are inside the cluster  $C$ , atom  $j$  is outside, and atom  $c$  represents the central atom in the calcu-

lation. The second term cancels double counting in the first term. The double counting comes from the fact that whenever the backscattering sequence ( $i-j-i$ ) occurs in the scattering path, then one should use  $\tilde{G}_{ij}^0 t_j G_{ji}^0$  instead of  $\tilde{G}_{ij}^0 t_j \tilde{G}_{ji}^0$ . In practice, it may be convenient simply to check for paths that extend outside a cluster  $C$  and use  $G^0$  or  $\tilde{G}^0$  as appropriate.

The total propagator  $G$  in Eq. (5), calculated as described above, can then be used to obtain the density of states—a necessary component for the SCF calculations. As illustrated in Eqs. (3) and (4), the imaginary part of  $G$  is of primary interest, but in order to do the integration in the complex energy plane we have to keep both the real and imaginary parts. Thus, for convenience, we define a reduced complex Green's function whose imaginary part is the local DOS,

$$g_i(\mathbf{r}, E) = -\frac{2}{\pi} G_i(\mathbf{r}, \mathbf{r}, E), \quad (16)$$

where  $\text{Im } g_i(\mathbf{r}, E) = \rho(\mathbf{r}, E)$ .

One of the advantages of the RSMS approach is that integration over energy can be done more efficiently in the complex energy plane. In our implementation we use only about 60–100 points on a rectangular contour  $C$  enclosing the occupied valence states. This contour  $C$  starts at a real energy  $E_c$  chosen above the energies of all core levels but below all valence states. The energy  $E_c$  in FEFF8 has a default core-valence separation  $E_c$  defined for each atom, but it can be easily overridden. The contour goes from  $E_c$  to  $E_c + iE_i$  to  $E_F + iE_i$ , and down to  $E_F + iT$ , where  $T$  lies just above the real axis. Typically we set  $E_i \approx 4$  eV and  $T = 0.025$  eV. We also search for the new Fermi level with a small imaginary part  $T$ . This value of  $T$  roughly simulates the effect of finite temperature ( $\approx 300$  K), since it leads to occupation numbers  $n(E) = (1/\pi) \arctan[(E - E_F)/T]$ , which are comparable to the Fermi-Dirac distribution, but with power-law rather than exponential tails.

The use of the term ‘‘valence states’’ in typical electronic structure calculations can differ from the usual meaning of ‘‘valence states’’ in chemistry, due to the overlap of the energy bands associated with these states. Thus, in our approach a state is defined to be core or valence, depending on whether its energy lies below or above  $E_c$ , which is typically 40 eV below  $E_F$ . For example, we consider the  $3d$  states in Cu to be valence states since they overlap strongly with  $3p$  and  $4s$  states.

Since we consistently use spherical symmetry in our present implementation, we obtain after spherical averaging

$$g_i(r, E) = \int \frac{d\Omega}{4\pi} g_i(\mathbf{r}, E) = \frac{k}{\pi^2} \sum_{L, \alpha} \{R_l^\alpha(r)^2 e^{2i\delta_l} G_{Ll, Li}(E) + (2l+1)R_l^\alpha(r)[N_l^\alpha(r) + iR_l^\alpha(r)]\}. \quad (17)$$

This procedure is carried out for each distinguishable site  $i$  in a solid or molecule. The space integration of  $\rho_i(r, E)$  then yields  $\rho(E)$ , the DOS. The Fermi level  $E_F$  is found iteratively by energy integration of the DOS. The energy integration of  $g_i(r, E)$  in the complex plane up to  $E_F$  then gives the new total electron density  $\rho_i(r)$ .

We regard the presently implemented space integration method as the least satisfactory approximation in our SCF loop and should be improved in subsequent code development. We are currently using an approach similar to the atomic sphere approximation (ASA).<sup>19</sup> Thus in the initial iteration, the Norman radii  $R^{nm}$  (i.e., the analog of the Wigner-Seitz radii of neutral spheres) are calculated, using the definition

$$\int_0^{R_i^{nm}} dr 4\pi r^2 \rho_i(r) = Z_i, \quad (18)$$

where  $Z_i$  is the charge of the  $i$ th nucleus. These Norman radii are kept fixed for all iterations. To obtain  $g_i(E)$  [and hence  $\rho_i(E)$ ] we then use

$$g_i(E) = \int_0^{R_i^{nm}} dr 4\pi r^2 g_i(r, E). \quad (19)$$

As in the ASA, our method double counts charge in the region where two Norman spheres overlap and does not count charge at all in the region not covered by any Norman sphere. This approximation might be intolerable for some ground-state calculations where very high accuracy is needed; however, it works well when the density is slowly varying and is a fairly good practical approximation to account for charge transfer within the RSMS approach in XAS calculations as described below. Next, we find the new density around the  $i$ th site in two ways. First we find the Fermi level from the relation

$$\text{Im} \int_C^{E_F} dE \sum_i N_i g_i(E) = N_{\text{el}}, \quad (20)$$

where  $N_i$  is the number of sites of  $i$ th type,  $N_{\text{el}}$  is the total number of electrons in the system, and  $C$  is the contour of integration. Next, we find the local Fermi level at the  $i$ th site by requiring no charge transfer from the  $i$ th Norman sphere:

$$\text{Im} \int_C^{E_{F,i}} dE g_i(E) = Z_i - q_i, \quad (21)$$

where  $q_i$  is the charge transfer from the previous iteration

$$q_i = Z_i - \int_0^{R_i^{nm}} dr 4\pi r^2 \rho^{\text{old}}(r), \quad (22)$$

initialized so that  $q_i$  is always zero before the first iteration. Thus, we construct two new densities, one of which includes the charge transfer while the other does not. The second is still useful since it includes changes in the valence wave functions:

$$\rho_{i,1}(r) = \text{Im} \int_C^{E_F} dE g_i(r, E), \quad (23)$$

$$\rho_{i,2}(r) = \text{Im} \int_C^{E_{F,i}} dE g_i(r, E). \quad (24)$$

If self-consistency is reached  $E_{F,i} = E_F$  and  $\rho_1 = \rho_2$ .

As is typical in SCF calculations, at least one convergence acceleration factor  $c$  is usually required to achieve stable convergence.<sup>19</sup> When one factor is used, the new density at

each iteration is computed as  $\rho_i^{\text{new}}(r) = (1 - c)\rho_i^{\text{old}}(r) + c\rho_{i,1}(r)$ . Typical values of  $c$  are about 0.2 or smaller. In our algorithm we enforce charge conservation by  $\rho_2$  and thus need two convergence acceleration factors in cases where significant charge transfer is possible:

$$\rho_i^{\text{new}} = (1 - c_1 - c_2)\rho_i^{\text{old}} + c_1\rho_{i,1} + c_2\rho_{i,2}. \quad (25)$$

For elements with narrow  $f$  bands, such as Pu and U discussed in Sec. III, we used  $c_1 = 0.02$  and found that a value of  $c_2 = 0.05$  was essential for swift convergence. Once the new density is calculated it is used to start a new iteration. This new  $\rho(r)$  is then used to calculate new scattering potentials and these steps are iterated to self-consistency. Typically 10 to 20 iterations are required to converge to a precision in  $E_F$  of a fraction of an eV. Sites with a core hole are treated similarly, except for a frozen core hole in a given core level. The SCF procedure will automatically fully screen the core hole. This approach yields a SCF treatment of core-hole relaxation analogous to the impurity KKR method used by Zeller and co-workers.<sup>20</sup>

We have implemented our SCF MS approach into an efficient *ab initio* RSMS code FEF8 for XANES calculations. In the remainder of this paper, we will discuss applications of our approach and its interpretation. Our code has many attractive properties compared to other methods:

(i) The code calculates XAS and DOS for arbitrary heterogeneous clusters of atoms throughout the periodic table, without any assumption of symmetry or periodicity.

(ii) The code is semiautomated with the same minimal input—i.e., atomic numbers and Cartesian coordinates that uniquely define system—as in previous versions of FEF7.<sup>6</sup> The code also uses the same spinor relativistic atomic code, energy-dependent self-energy (e.g., the HL potential) and complex semirelativistic phase shift algorithms as in FEF7.

(iii) The code determines SCF MT potentials in the presence (or absence) of a screened core hole using the RSMS method based on complex plane Green's-function calculations, rather than wave functions.

(iv) The full multiple scattering calculations of  $G^{\text{SC}}$  are done by matrix inversion using a single precision lower-upper decomposition algorithm<sup>21</sup> and exact RA separable propagators  $G^0$ .

(v) The code approximates the effects of thermal disorder for FMS calculations.

In contrast to other XANES codes, our approach also yields electronic structure information in the form of LDOS and charge counts. However, the energy resolution and accuracy of our DOS calculations is limited by broadening due to cluster size and core-hole lifetime and by the lack of full potential corrections to the MT potentials. Thus, while our results for DOS lack the fine details of modern band-structure calculations, the resolution inherent in our approach is appropriate for XANES spectra. Moreover, integrated quantities such as the total density, Fermi energy, and charge transfer are not expected to be sensitive to fine details in the DOS. Thus, we feel that the present accuracy is sufficient both for a quantitative treatment of XANES and its interpretation in terms of electronic structure.

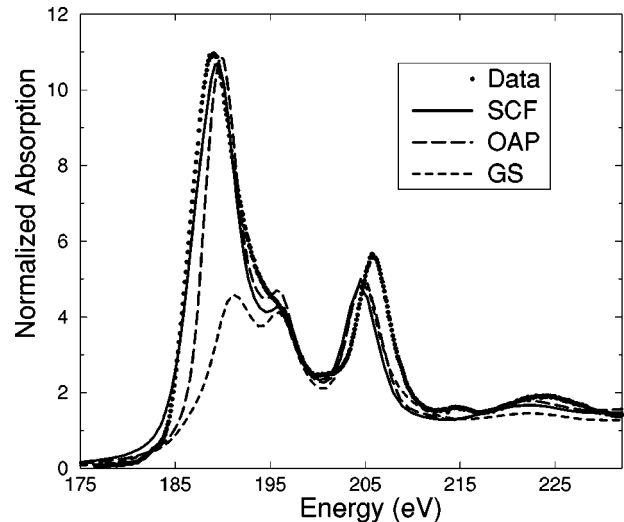


FIG. 1. XANES  $\mu(E)$  of cubic BN for an 87-atom cluster as calculated in this work with SCF (solid line) and with OAP (long dashes) potentials and compared to experimental ELNES data (dots). Calculations were made with the final-state rule, i.e., with a fully relaxed core hole. Both calculations reproduce the large white-line intensity, but the white-line width is better with SCF. The calculation using the ground-state potential (short dashes) lacks the strong white line.

### III. APPLICATIONS

We now present several applications of our approach for quantitative XANES and DOS calculations. Our goal is to test the validity of our approach by comparisons both with accurate electronic structure theory and with experiment. In particular we aim to examine the effects of self-consistency and FMS on calculations both of XAS and DOS. The SCF loop described above can also be applied to a full potential calculation, and we plan to address such corrections to the MT approximation in future work. ‘Near-field’ corrections<sup>22</sup> due to the use of overlapping geometry and various exchange-correlation potential corrections will also be addressed later, since they represent less serious approximations.

#### A. XANES and DOS of cubic BN

As a first example we treat the  $K$ -shell XANES and DOS of cubic BN, which crystallizes in the zinc sulfide structure. The spectrum of BN is a challenge for our code, as the spherical averaging around each atom is not well justified for such an open lattice. Because the first coordination shell about each atom forms a tetrahedron, the potential lacks inversion symmetry. It is not obvious *a priori* that the SCF potentials using ASA and spherical averaging would improve on the simple, non-self-consistent overlapped atomic potentials (OAP's) used in FEF7 for such open systems.

The results of our calculations are compared to experiment in Fig. 1 with SCF (solid) and OAP's (long dashes). Both the SCF and OAP calculations are carried out with the final-state rule; i.e., the photoelectron wave function is calculated with a fully relaxed potential in the presence of a core hole in the  $1s$  state. Both XANES calculations were done on an 87-atom cluster and compared to the results from

TABLE I. The electron number counts for  $s$ ,  $p$ ,  $d$ , and  $f$  electrons and the differentially calculated charge transfer  $q_i$ , defined in Eq. (22), for the cubic BN and  $\text{UF}_6$  molecule. The last two lines are the occupation numbers and charge transfer for  $\text{UF}_6$  calculated with the GAUSSIAN code (Ref. 26).

Element	$s$	$p$	$d$	$f$	$q_i$
B	0.83	1.71	0.34		+0.12
N	1.52	3.50	0.11		-0.12
U	0.37	6.21	1.71	3.02	+0.66
F	1.96	5.04	0.07	0.05	-0.11
U	0.20	6.30	1.40	1.70	+2.40
F	1.90	5.50			-0.40

electron-energy-loss near-edge structure (ELNES) experiment.<sup>25</sup> No adjustable parameters were used in the calculations except for 1.3-eV broadening to account for the experimental ELNES energy resolution and an energy shift of 6 eV to match the experimental threshold. Note that the Fermi level  $E_F$  is accurately determined by our SCF method to within about 1 eV based on the shape of the white line. The SCF potentials used were calculated on smaller clusters of 29 atoms in 20 iterations with nonoverlapping MT's, a 1s core hole, and a basis of  $s$ -,  $p$ -, and  $d$ -scattering states at each site, hence requiring the inversion of  $(261 \times 261)$  matrices at each energy point. The calculated occupation numbers and charge transfers are shown in Table I.

We have found that a fully relaxed core hole is essential to obtain agreement with experiment for BN, since the intensity of a white line is much smaller for ground-state potentials and indeed the shape of the XANES spectrum is quite different, as shown by the short-dashed line in Fig. 1. Thus, the final-state rule works well for BN, and the influence of the core hole leads to a strong enhancement of the spectrum close to the edge for both SCF and non-SCF potentials. Moreover, we see that the fine structure in the  $p$ DOS with a core hole in Fig. 2 is similar to that in the observed XANES. The width of the white line is improved using the SCF potential rather than the OAP's. The experimental full width at half maximum (FWHM) is 7.1 eV, while the calculated FWHM with SCF is 6.2 eV and that with OAP's is 4.9 eV. A small discrepancy between the amplitude of the second large peak may be due to errors in the theory; for example, errors in the self-energy or the neglect of nonspherical corrections to the potential. Part of this discrepancy may be due to differences in energy dependence of the atomic background function  $\mu_0(E)$  in Eq. (1) in ELNES and XANES.<sup>24</sup>

To assess the quality of our calculation relative to modern band-structure methods, we show in Fig. 2 the corresponding  $p$ DOS with and without a core hole and, for comparison, the results of a linear combination of muffin-tin orbitals (LMTO's) calculation<sup>19</sup> broadened by 1.3 eV. These results show that even for relatively small clusters ( $N \approx 50$ –100 atoms) our RSMS approach for the ground state yields reasonable agreement with a broadened crystal calculation. This is reassuring since our approach differs from the LMTO approach in several respects. For example, in our approach no energy linearization is used nor do we introduce empty spheres to correct for errors in the MT potentials in open structures. Note in particular the large downward shift in

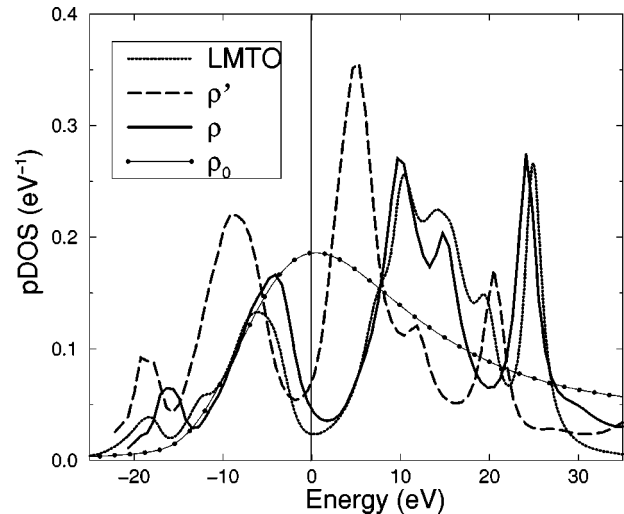


FIG. 2.  $p$ DOS  $\rho(E)$  of cubic BN for an 87-atom cluster as calculated in this work (solid line) and from LMTO calculations broadened by 1.3 eV (dotted). Notice the gap in  $\rho(E)$ , which is formed by the effect of  $\chi(E) \sim -1$  on  $\rho_0(E)$  (thin solid with circles), the atomic DOS. Also shown is the  $p$ DOS in the presence of a core hole  $\rho'(E)$  (dashed). The vertical line at  $E=0$  represents the Fermi level as calculated for  $\rho(E)$  and  $\rho'(E)$  and is the center of the band gap in the broadened LMTO calculation.

energy of the DOS spectrum due to the presence of the (attractive) core hole. These results show clearly that a screened core-hole potential is essential to obtain satisfactory XANES for BN. Figure 2 also demonstrates that it is inappropriate to interpret XAS in terms of the ground-state DOS since the core hole changes the XANES spectrum and DOS dramatically near the Fermi energy. This also shows that *ab initio* calculations of DOS with and without a core hole are necessary to draw conclusions about the ground-state electronic structure from an XAS measurement.

## B. DOS of $\text{UF}_6$

We now test the relativistic electronic structure algorithms in our code against accurate full potential (i.e., non-muffin-tin) ground-state quantum chemistry calculations using the GAUSSIAN code.<sup>25</sup> We aim to demonstrate that our SCF DOS calculations for the heterogeneous molecular system  $\text{UF}_6$  represent an improvement over those calculated with OAP's, and are in good agreement with full potential calculations except for small energy shifts. We also evaluate and compare charge-transfer calculations between the two methods.

The total ground-state DOS for the  $\text{UF}_6$  molecule is shown by the solid line in Fig. 3. These results include 2-eV Lorentzian broadening. It is clear from the peak intensities and positions that the SCF DOS is a significant improvement over the OAP DOS. For example, the energy of the F 2p electron is much closer to the energy of the U 5f states, but the GAUSSIAN code finds these states slightly closer to each other. Notice too that the peaks at lower energies (F 2s and U 6p states) have nearly the same amplitudes and positions as with the GAUSSIAN code. This is probably due to the localization of these states, since the ASA is expected to work better for localized than for delocalized electrons and our

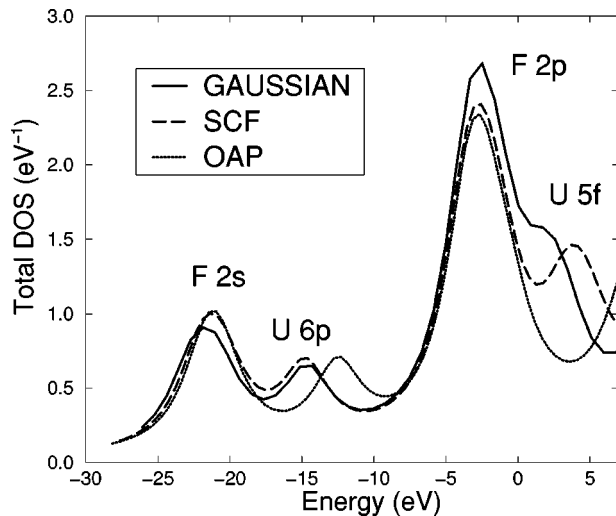


FIG. 3. Total DOS for the  $\text{UF}_6$  molecule from the GAUSSIAN (Ref. 26) code (solid) compared with our SCF (long dashes) and OAP (dashes) calculations. The SCF potentials provide a significant improvement over the OAP. The discrepancy between our SCF and GAUSSIAN results is likely due to the neglect of nonspherical corrections. To compensate for shifts in absolute energies, the SCF calculation was shifted to the right by +2.9 eV and the OAP calculation by +5.2 eV.

SCF Dirac-Fock atom calculations are highly accurate. Our calculations reproduce all the main features in the DOS of  $\text{UF}_6$ , although a shift in absolute energy of 2.9 eV was needed to align the peaks from the SCF calculation with the GAUSSIAN calculation. This shift in absolute energy is probably due to outer-sphere effects and MT corrections. The absolute energy scale of OAP calculation was even further off, requiring a shift of 5.2 eV. Despite the improvement of the SCF potentials over the OAP's, the discrepancies suggest that further refinements in the potentials are still needed.

The  $\text{UF}_6$  molecule represents a case where the assignment of formal oxidation states is unambiguous, i.e., F is in oxidation state  $-1$  and U is in  $+6$ . Hence this system is a well-defined case for comparisons of the relation between the oxidation state and the charge transfer  $q_i$ . In our code this quantity  $q_i$  in Eq. (22) is calculated differentially, i.e., as a difference between the atomic overlap charge density and the SCF density within a Norman sphere. We feel that this is an improvement on definitions of charge associated with each ion in a compound based upon an arbitrary partitioning of space. We also report the electron counts (occupation numbers) obtained by integrating the local density of states to the Fermi energy. The interesting result is that the charge transfer calculated differentially is about an order of magnitude smaller than that given by formal oxidation state considerations, although these quantities are well correlated. The charge transfer and electron counts obtained with our code are shown for  $\text{UF}_6$  in Table I. For comparison, Hay *et al.*<sup>26</sup> report  $\text{U}^{+2.4}$ :  $6p^{6.0}6d^{1.45}f^{1.77}s^{0.27}p^{0.3}$  and  $\text{F}^{-0.4}$ :  $2s^{1.92}2p^{5.5}$  for the occupancy and charge transfer. The GAUSSIAN code uses a linear combination of atomic orbitals to construct molecular orbitals, and the occupation numbers correspond to the weight of each atomic orbital in the total electron density. Thus, the GAUSSIAN code does not use a differential charge-transfer calculation, since the atomic orbitals may have non-

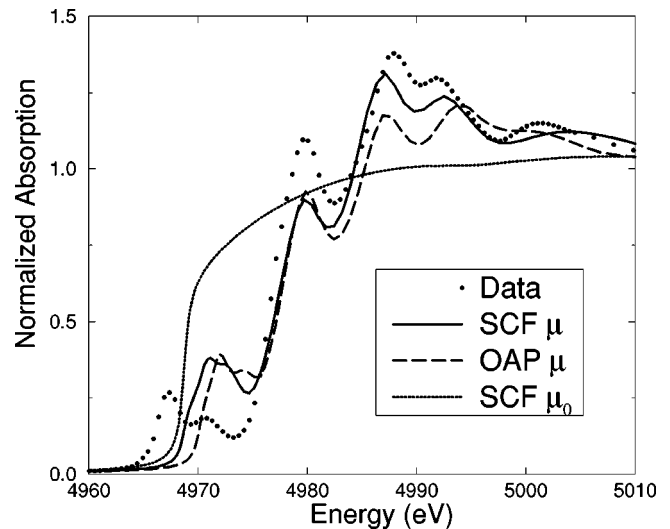


FIG. 4. Effect of self-consistency on the XANES of  $\text{PbTiO}_3$ . The calculations using the SCF potentials (solid line) agree better with transmission XAS data, measured at 15 K (big dots), than with calculations using OAP (long dashes). The atomic background,  $\mu_0(E)$  in Eq. (1), from the SCF calculations is also shown (dotted line). The calculations were shifted by 4.5 eV to match the absolute energy scale of the data.

zero density near the neighboring atoms. However, the occupation numbers and charges transfers calculated with the GAUSSIAN code are well correlated with our calculations, as shown in Table I. Except for the  $f$  occupancy, the electronic configurations are seen to be quite similar.

### C. XANES of $\text{PbTiO}_3$

To illustrate the applicability of our approach to structurally complex systems, calculations were made for a 147-atom cluster of tetragonal, uniaxially distorted  $\text{PbTiO}_3$ , with up to  $p$ ,  $d$ , and  $f$  electron basis sets for O, Ti, and Pb, respectively. This system provides a good test of two objectives of this paper, the effect of SCF potentials on XANES and the utility of a RSMS approach. The fully distorted structure is the reported crystal structure<sup>27</sup> in which the central Ti atoms are uniaxially displaced from centrosymmetric sites by 0.311 Å. The strong effect of self-consistency on the calculation is shown in Fig. 4. Two calculations were done for the same cluster of 147 atoms, with the only difference between them being the use of SCF or OAP potentials. Clearly the SCF calculation agrees better with experiment.

At 763 K,  $\text{PbTiO}_3$  undergoes a transition between crystallographically tetragonal and cubic phases.<sup>27</sup> From analysis of the EXAFS of  $\text{PbTiO}_3$ , it has been found<sup>28</sup> that the local structure around the Ti atom remains distorted well into the crystallographically cubic phase. The presence of this distortion is readily apparent in the high-temperature data as the first “edge peak” above the Fermi energy does not disappear or become small as in centrosymmetric structures.<sup>29</sup> The dependence of this peak on the distortion of the Ti atom is evident in our calculations. In Fig. 5 we show calculations of both the uniaxially distorted and undistorted (cubic perovskite) structures. The strong dependence of the XANES on the local distortion is clearly seen not only in the first edge peak above the Fermi energy observed at 4966 eV (the peak

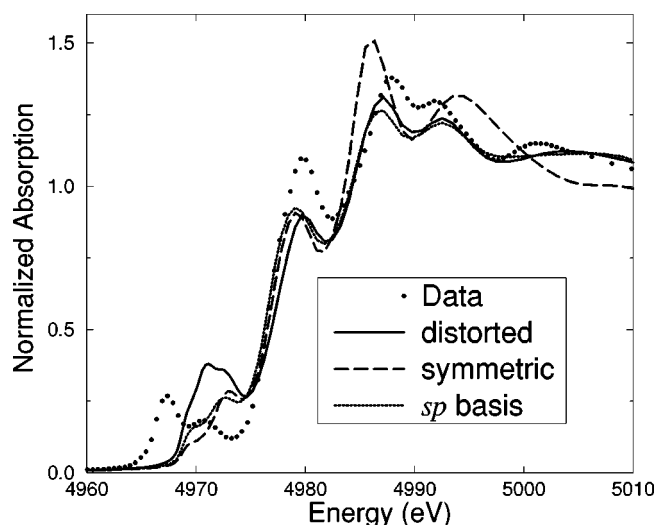


FIG. 5. Effect of structural distortion on Ti  $K$ -edge XANES in  $\text{PbTiO}_3$ . Shown are XANES calculations of the distorted crystal structure (Ref. 27) (solid line), an ideal model with Ti and O at centrosymmetric sites (dashes), and for comparison, transmission XAS data (circles). The area added to the edge peak near 4966 eV is found to be proportional to the mean-square displacement of the Ti atom from the midpoint of the oxygen octahedron. Calculations with only  $s$  and  $p$  electrons for the central atom (dotted) and for the distorted structure demonstrate that the intensity of this peak is due to hybridization between the  $p$  and  $d$  electrons of the absorbing Ti.

is at 4970 eV in our calculation) but in the entire spectrum. For example, the dominant post edge peak at 4986 eV and the XAFS amplitude  $\chi$  are clearly too large when calculated for the centrosymmetric structure. However, the reduction of intensity in the first edge peak at 4970 eV is the most dramatic effect of neglecting the uniaxial distortion in the calculation. The intensity of this peak has a strong dependence on the  $d$  states of the absorbing Ti atom. To demonstrate this we made the XANES calculation, including only  $s$  and  $p$  electrons of the absorbing atom in the distorted structure but with the same SCF potential. This is shown by the dotted line in Fig 5. Without the central atom  $d$  electrons the first peak is strongly suppressed. This implies that this intensity arises due to hybridization between the  $p$  and the  $d$  orbitals of the absorber, an effect that is forbidden for centrosymmetric structure but increased by local distortions.

There still remain some differences between our SCF FMS calculations and the details of the XAS “edge” structure just above  $E_F$ . This may again indicate problems with the potentials or possibly the assumed local distortions. We note that the region just above the Fermi energy exhibits very strong scattering, i.e.,  $\chi(E) \sim -1$  in Eq. (1), and thus a very small DOS, which is sensitive to the nature of the  $d$ DOS and the deviation from centrosymmetry.

#### D. XANES of Pu hydrates

In this example we demonstrate the applicability of our approach to calculations of the excitation threshold energy. The excitation threshold is the Fermi energy  $E_F$ , which, on the absolute photoelectron energy scale, is usually referred to as  $E_0$  in the EXAFS literature. In this section, we will use  $E_F$  to refer to a calculated threshold energy, and  $E_0$  to refer to

that obtained from EXAFS analysis. One might expect that the effect of the SCF potentials on the calculated EXAFS spectrum will be small since the extended spectrum typically starts about 40 eV above the Fermi energy and hence is only weakly sensitive to chemical effects such as the fine details of the potential. Indeed, we have found rather generally that the overall shape of the calculated fine structure  $\chi$  is insensitive to effects of self-consistency, even much closer to the edge. However, the neglect of charge transfer and crude estimates of the Fermi level, as in previous XAS codes,<sup>1,6</sup> can still have large effects on EXAFS analysis. For example, a larger number of variable parameters are typically required when using a non-self-consistent calculation as a fitting standard. Also, since  $E_0$  is correlated with interatomic distances in a fit, the need to fit  $E_0$  results in larger uncertainties in extracted parameters. In the EXAFS analysis of a heterogeneous material, the neglect of charge transfer may require separate  $E_0$ 's for each type of atom as variable phase corrections in a fit. For example, Haskell *et al.*<sup>30</sup> used four different values of  $E_0$  to fit the La and Sr  $K$ -edge EXAFS in  $\text{La}_{1-x}\text{Sr}_x\text{CuO}_4$ . Extrapolating an estimate for  $E_0$  determined in the EXAFS region to the near-edge region may also be inaccurate due to errors in the self-energy model and in the calculated Fermi level in the fitting standard. The latter error could be sensitive to the effect of charge transfer. However, if the fitting standard accounts for charge transfer and accurately determines the Fermi level, then the  $E_0$  correction should be the same for different atoms, and physically meaningful fits should use a single  $E_0$  parameter even for heterogeneous materials.

In Fig. 6(a) we show XANES data for Pu hydrates with the Pu in four different oxidation states from 3+ to 6+. For each of these data, the experimental EXAFS data<sup>31</sup> were analyzed to determine an empirical value for  $E_0$ , using a non-linear least-squares-fitting code.<sup>32</sup> The fits were performed twice, once with amplitudes and phases obtained from FEFF7's OAP calculation and again using the SCF potentials from FEFF8. The location of  $E_0$  from the optimized fits are shown in Fig. 6(a), with OAP results represented by circles and SCF results by squares. For comparison we show in Fig. 6(b) the values for  $E_F$  calculated directly using the SCF potentials and Eq. (20). Note that the empirically determined Fermi levels using FEFF8 fitting standards are very close to those directly calculated by FEFF8 for  $\text{Pu}^{3+}$  and  $\text{Pu}^{4+}$ , as seen in Figs. 6(a) and 6(b). However, the Fermi energies determined empirically and theoretically for  $\text{Pu}^{5+}$  and  $\text{Pu}^{6+}$  differ by about 13 eV, although the empirical determinations using the SCF fitting standards of FEFF8 are significantly improved over those from OAP standards. Although the values of  $E_F$  calculated using our SCF potentials appear to be reliable even for the higher valence states of Pu, improvements to the fitting standards are required. As seen by the high values of  $E_0$  for  $\text{Pu}^{5+}$  and  $\text{Pu}^{6+}$  in Fig. 6(a), unphysical phase corrections are still needed in fits to the EXAFS data in these cases. The different behaviors of the  $\text{Pu}^{3+}$  and  $\text{Pu}^{4+}$  relative to  $\text{Pu}^{5+}$  and  $\text{Pu}^{6+}$  can be understood in terms of their structures.  $\text{Pu}^{3+}$  and  $\text{Pu}^{4+}$  are surrounded by nine and eight nearly equidistant water ligands. Consequently, the spherical averaging of the densities and potentials performed by FEFF8 is a reasonable approximation. However,  $\text{Pu}^{5+}$  and  $\text{Pu}^{6+}$  both possess plutonyl oxygen atoms along one axis, which are much

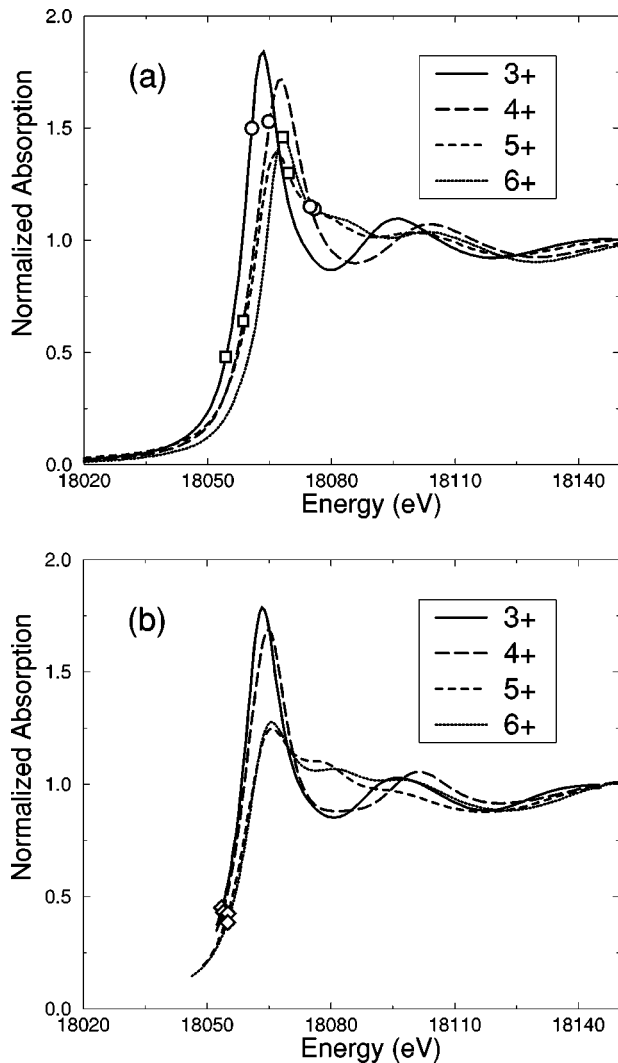


FIG. 6. (a) Experimental XANES of Pu hydrates with formal oxidation states from +3 to +6. The positions of the Fermi level, obtained by fitting the EXAFS using fitting standards from the SCF FEFF8 code (squares) are more accurate than those obtained from a non-SCF OAP calculation FEFF7 (circles). (b) Calculated XANES of Pu hydrates with FEFF8, without any adjustable parameters. The diamonds show the theoretical positions of the Fermi level. All features of the experimental XANES for each hydrate are reproduced, including the variation of white-line intensity with formal oxidation state. However, relative edge positions are reproduced only qualitatively.

closer to the Pu than the remaining oxygen atoms located in a plane orthogonal to that axis. This strong coordinational asymmetry makes the validity of spherical averaging questionable. Again MT corrections or full potential calculations may be required for better agreement.

For  $\text{Pu}^{3+}$  and  $\text{Pu}^{4+}$ , the white line intensity calculated with our FEFF8 code agrees well with experiment. The main difference between previous simulations of the Pu hydrates<sup>33</sup> using FEFF7 and the current ones using SCF code FEFF8 is that no adjustment of  $E_F$  was needed. Also, our calculations with FEFF8 used the Hedin-Lundqvist self-energy, while with FEFF7 we needed a nonlocal self-energy model to get adequate agreement with experiment. Without better potential models, however, it is difficult to make definite conclusions

about the validity of different self-energy models, since the potentials and the self-energies can have comparable effects on XANES.

#### IV. XANES INTERPRETATION

We now turn to an interpretation of XANES based on an EXAFS-like scattering theoretic framework. This interpretation is based on the premise that all XANES features are due to electron scattering. We believe that this picture provides a useful and intuitive alternative to interpretations based, for example, on molecular orbitals.<sup>2</sup> The main ingredients of this interpretation are the atomic background functions  $\rho_0$  or  $\mu_0$ , and the oscillatory XAFS functions  $\chi(E)$  in Eq. (1). Both of these quantities have well-known structural interpretations. By analogy with the now well-accepted interpretation of EXAFS we arrive at the following observations:

**LDOS and XANES.** Because the atomic background terms  $\rho_0$  and  $\mu_0$  are generally smooth above threshold, all the fine structure in the LDOS and XANES arises from the electron-scattering contribution in  $\chi(E)$  while peak heights are also proportional to  $\rho_0$  or  $\mu_0$ . The XANES spectrum corresponds to the final-state LDOS calculated in the presence of a screened core hole.

**Threshold.** The threshold for XANES and EXAFS is the Fermi level  $E_F$  (or  $E_0$  on an absolute scale), which lies below all “edge structure.” Thus,  $E_0$  is not necessarily the midpoint of the main rise in the XANES. SCF calculations are usually needed to obtain accurate Fermi energies.

**Edge structure.** The “edge structure” in XANES is controlled largely by the magnitude of the XAFS function  $\chi$ . For large positive  $\chi$ , the edge exhibits a “white line,” while for large negative  $\chi(E) \sim -1$  the absorption is small, corresponding to a gap or pseudo gap in the LDOS, i.e., a “dark line.” A negative  $\chi$  implies that there is *destructive interference* between the outgoing photoelectron wave and the waves backscattered from neighboring atoms. FMS calculations are required when  $|\chi|$  is not small compared to unity.

**Disorder.** Thermal and structural disorder lead to a Debye-Waller-like reduction in the amplitude of the fine structure  $|\chi|$ , which can be discussed in terms of intermediate range order.<sup>17</sup> A decrease in  $|\chi|$  corresponds to a reduction in white-line amplitude ( $\chi \geq 0$ ) or an increase in the LDOS in a gap ( $\chi \leq 0$ ).

This interpretation is illustrated well by our examples. The connection between LDOS and XANES is discussed for BN in Sec. III A. For this case, as is typical in insulators, the Fermi energy  $E_0$  is found to lie roughly in the middle of the band gap in the density of states, a few eV below the rise in the main edge (Fig. 1). Similarly for the EXAFS analysis of  $\text{PbTiO}_3$ , the correct Fermi level lies below the small edge peaks and well below the main rise. The XANES spectrum between  $E_0$  and the main rise is sometimes termed the “pre-edge region,” but we feel that “edge region” is better terminology since the Pauli principle precludes absorption before the true threshold ( $E_F$ ). By analogy with the historical use of “white line” to denote a large peak in the absorption at the edge, the term “dark line” aptly describes a pronounced reduction at an absorption edge. Materials such as BN or  $\text{PbTiO}_3$  both exhibit pseudo gaps in the  $\rho$ DOS and hence good examples of “dark lines.” The small peaks in

the edge region of  $\text{PbTiO}_3$  (Fig. 5) have been interpreted in terms of  $p$ - $d$  hybridization due to the breakdown of centro symmetry, and are seen to increase in magnitude with increasing disorder (i.e., with decreasing  $|\chi|$ ).

Of course, our XAFS-like picture of the XANES does not contradict the molecular-orbital picture. It simply represents an alternative but equivalent interpretation of the underlying physics. Depending on the situation, one or the other may be more appropriate. For a discussion of peak splitting in these spectra, the molecular-orbital picture may provide a more natural language in terms of electron states. The scattering theoretic picture, which is natural in the EXAFS region, seems more appropriate to interpret the structural origin of XANES and effects of thermal disorder.

## V. CONCLUSIONS

We have presented an approach for excited state x-ray spectroscopy calculations that combines simultaneous RSMS calculations of electronic structure and XAS. The method improves upon most current cluster calculations of XAS by using SCF potentials. We have implemented these SCF potentials along with a full MS treatment of XANES into the FEFF program (version 8). We have found that SCF potentials are essential for an accurate determination of the Fermi level and also for calculations of charge transfer between atoms. FMS calculations are necessary in XANES when the amplitude of the fine structure  $|\chi|$  is not small compared to unity. When FMS is important, the code also permits calculations for bigger clusters than previously possible by combining an accurate FMS calculation for a small cluster and a high-order MS path expansion for paths that extend outside. Our RSMS method compares favorably to many currently available electronic-structure methods since it is a relativistic, all-electron method applicable to general systems throughout the periodic table without the need for symmetry or periodicity, Brillouin-zone sums, supercells, pseudopotentials, or energy linearization approximations. On the other hand, the LDOS calculated with our approach is broadened due to finite-size effects, and presently the code lacks outer-sphere, empty sphere, and nonspherical corrections to the MT potentials.

Additionally, our method incorporates self-consistent core-hole relaxation (the final-state rule), an energy-dependent self-energy (usually the HL model<sup>13</sup>), as well as effects of correlated vibrations and disorder, all of which are important for a quantitative description of XANES. Several applications have been presented to show that SCF calculations of XANES are in better agreement with experimental data than those with overlapped atom potentials. We have also presented a structural interpretation of XANES analogous to the conventional interpretation of EXAFS. Finally, the code implementing our method is semiautomated, thereby making XAS calculations and the interpretation of spectral features in terms of geometrical and electronic structure readily accessible.

Although we have restricted our discussion to XANES, the RSMS method can be generalized to many other spectroscopies, e.g., x-ray emission spectroscopy (XES), x-ray photoelectron diffraction,<sup>34</sup> and anomalous x-ray scattering,<sup>35</sup> x-ray magnetic circular dichroism,<sup>36</sup> etc. Many extensions and improvements are still desirable, e.g., a more accurate treatment of nonspherical corrections to the potentials,<sup>37</sup> outer-sphere corrections in molecules, and many-body and core-hole screening effects, and we hope to address many of these limitations in future work.

## ACKNOWLEDGMENTS

The authors thank M. Jaouen and G. Hug for making available their experimental data, O. Jepsen and O. K. Andersen for providing the LMTO code used here, and R. L. Martin for providing the energy levels of the  $\text{UF}_6$  molecule calculated with the GAUSSIAN code. We also thank them and R. C. Albers, C. Brouder, G. E. Brown, F. Farges, T. Fujikawa, M. Newville, D. Saldin, T. Sikora, E. L. Shirley, E. A. Stern, and J. Wills for comments. One of us (J.J.R.) thanks M. Jaouen and the Univ. of Poitiers for generous hospitality where part of this work was carried out. This work was supported in part by the U.S. Department of Energy, Grant Nos. DE-FG03-97ER45623 (J.J.R.) and DE-FG06-90ER45425, the National Research Council (B.R.), and by Los Alamos National Laboratory (A.L.A. and S.D.C.).

<sup>1</sup>See, for example, P. J. Durham, J. B. Pendry, and C. H. Hodges, *Comput. Phys. Commun.* **25**, 193 (1982); D. D. Vvedensky, D. K. Saldin, and J. B. Pendry, *ibid.* **40**, 421 (1986); D. E. Ellis and G. L. Goodman, *Int. J. Quantum Chem.* **25**, 185 (1984); T. A. Tyson, K. O. Hodgson, C. R. Natoli, and M. Benfatto, *Phys. Rev. B* **46**, 5997 (1992); Z. Y. Wu, G. Ouvrard, P. Gressier, and C. R. Natoli, *ibid.* **55**, 10 382 (1997).

<sup>2</sup>J. Stöhr, *NEXAFS Spectroscopy* (Springer, Heidelberg, 1992).

<sup>3</sup>J. L. Beeby, *Proc. R. Soc. London, Ser. A* **302**, 113 (1967); P. Lloyd and P. V. Smith, *Adv. Phys.* **21**, 69 (1972); W. L. Schaich, *Phys. Rev. B* **8**, 4028 (1973); B. L. Gyorffy and M. J. Stott, *Band Structure Spectroscopy of Metals and Alloys* (Academic, New York, 1973); I. V. Bazhin, A. B. Kolpachev, and I. Ya. Nikiforov, *Phys. Status Solidi B* **156**, 309 (1989).

<sup>4</sup>P. A. Lee and J. B. Pendry, *Phys. Rev. B* **11**, 2795 (1975); C. A. Ashley and S. Doniach, *ibid.* **11**, 1279 (1975).

<sup>5</sup>J. E. Müller, O. Jepsen, and J. W. Wilkins, *Solid State Commun.* **42**, 365 (1982); R. C. Albers, A. K. McMahan, and J. E. Muller, *Phys. Rev. B* **31**, 3435 (1985).

<sup>6</sup>A. L. Ankudinov and J. J. Rehr, *Phys. Rev. B* **56**, R1712 (1997); S. I. Zabinsky, J. J. Rehr, A. Ankudinov, R. C. Albers, and M. J. Eller, *ibid.* **52**, 2995 (1995); and references therein. For further details see, for example, the documentation at the URL: <http://leonardo.phys.washington.edu/feff/>

<sup>7</sup>X.-G. Zhang and A. Gonis, *Phys. Rev. Lett.* **62**, 1161 (1989).

<sup>8</sup>J. J. Rehr, C. H. Booth, F. Bridges, and S. I. Zabinsky, *Phys. Rev. B* **49**, 12 347 (1994).

<sup>9</sup>J. J. Rehr, W. Bardyszewski, and L. Hedin, *J. Phys. IV* **7**, C2-97 (1997).

<sup>10</sup>K. H. Johnson, *Adv. Quantum Chem.* **7**, 143 (1973).

<sup>11</sup>L. Mattheiss, *Phys. Rev.* **133**, A1399 (1964).

<sup>12</sup>U. von Barth and L. Hedin, *J. Phys. C* **5**, 1629 (1972).

- <sup>13</sup>L. Hedin and S. Lundqvist, *Solid State Phys.* **23**, 1 (1969); B. I. Lundqvist, *Phys. Kondens. Mater.* **6**, 193 (1967); J. Mustre de Leon, J. J. Rehr, S. I. Zabinsky, and R. C. Albers, *Phys. Rev. B* **44**, 4146 (1991).
- <sup>14</sup>D. D. Koelling and B. N. Harmon, *J. Phys. C* **10**, 3107 (1977).
- <sup>15</sup>J. J. Rehr and R. C. Albers, *Phys. Rev. B* **41**, 8139 (1990).
- <sup>16</sup>F. Manar and C. Brouder, *Physica B* **208&209**, 79 (1995); D. Sebilliau, *J. Phys.: Condens. Matter* **7**, 6211 (1995).
- <sup>17</sup>F. Farges, G. E. Brown, Jr., and J. J. Rehr, *Phys. Rev. B* **56**, 1809 (1997).
- <sup>18</sup>T. Fujikawa, *J. Phys. Soc. Jpn.* **62**, 2155 (1993); T. Fujikawa *et al.*, *ibid.* **66**, 257 (1997).
- <sup>19</sup>O. K. Anderson, O. Jepsen, and M. Sob, *Electronic Band Structure and Its Applications*, edited by M. Yussouff (Springer-Verlag, Berlin, 1986); H. L. Skriver, *The LMTO Method, Muffin-Tin Orbitals and Electronic Structure* (Springer, Berlin, 1984).
- <sup>20</sup>P. J. Braspenning, R. Zeller, A. Lodder, and P. H. Dederichs, *Phys. Rev. B* **29**, 703 (1984).
- <sup>21</sup>E. Anderson *et al.*, *LAPACK Users' Guide* (Society for Industrial and Applied Mathematics, Philadelphia, 1995).
- <sup>22</sup>J. S. Faulkner, *Phys. Rev. B* **19**, 6186 (1979).
- <sup>23</sup>M. Jaouen, G. Hug, V. Gonner, G. Demazcau, and G. Tourillon, *Microsc. Microanal. Microstruct.* **6**, 127 (1995).
- <sup>24</sup>M. Qian, M. Sarikaya, and E. A. Stern, *Ultramicroscopy* **68**, 163 (1997).
- <sup>25</sup>P. J. Hay and R. L. Martin, *J. Chem. Phys.* (to be published); R. L. Martin (private communications).
- <sup>26</sup>P. J. Hay, W. R. Wadt, L. R. Kahn, R. C. Raffanetti, and D. H. Phillips, *J. Chem. Phys.* **71**, 1767 (1979).
- <sup>27</sup>R. J. Nelmes and W. F. Kuhs, *Solid State Commun.* **54**, 721 (1985).
- <sup>28</sup>N. Sicron, B. Ravel, Y. Yacoby, E. A. Stern, F. Dogan, and J. J. Rehr, *Phys. Rev. B* **50**, 13 168 (1994); B. Ravel, N. Sicron, Y. Yacoby, E. A. Stern, F. Dogan, and J. J. Rehr, *Ferroelectrics* **164**, 265 (1995).
- <sup>29</sup>B. Ravel and E. A. Stern, *Physica B* **208&209**, 316 (1995).
- <sup>30</sup>D. Haskel, E. A. Stern, D. G. Hinks, A. W. Mitchell, J. D. Jorgensen, and J. I. Budnick, *Phys. Rev. Lett.* **76**, 439 (1996); D. Haskel, E. A. Stern, D. G. Hinks, A. W. Mitchell, and J. D. Jorgensen, *Phys. Rev. B* **56**, R521 (1997).
- <sup>31</sup>S. D. Conradson, I. Al Mahamid, D. L. Clark, N. J. Hess, E. A. Hudson, M. P. Neu, P. D. Palmer, W. H. Runde, and C. D. Tait, *Polyhedron* **17**, 599 (1998).
- <sup>32</sup>S. D. Conradson (private communication).
- <sup>33</sup>A. L. Ankudinov, S. D. Conradson, J. Mustre de Leon, and J. J. Rehr, *Phys. Rev. B* **57**, 7518 (1998).
- <sup>34</sup>C. S. Fadley, in *Synchrotron Radiation Research: Advances in Surface Science*, edited by R. Z. Bachrach (Plenum, New York, 1991); A. P. Kaduwela, D. J. Friedman, and C. S. Fadley, *J. Electron Spectrosc. Relat. Phenom.* **57**, 223 (1991).
- <sup>35</sup>H. Stragier, J. O. Cross, J. J. Rehr, L. B. Sorensen, C. E. Bouldin, and J. C. Woicik, *Phys. Rev. Lett.* **69**, 3064 (1992).
- <sup>36</sup>A. L. Ankudinov and J. J. Rehr, *Phys. Rev. B* **56**, R1712 (1997).
- <sup>37</sup>C. R. Natoli, D. K. Misemer, S. Doniach, and F. W. Kutzler, *Phys. Rev. A* **22**, 1104 (1980).